Reconstruction in PET Cameras with Irregular Sampling and Depth of Interaction Capability*

P.R.G. Virador, W.W. Moses, *Senior Member, IEEE*, R.H. Huesman, *Senior Member, IEEE*

Lawrence Berkeley National Laboratory, University of California, Berkeley, CA 94720

Abstract

We present 2D reconstruction algorithms for a rectangular PET camera capable of measuring depth of interaction (DOI). The camera geometry leads to irregular radial and angular sampling of the tomographic data. DOI information increases sampling density, allowing the use of evenly spaced quarter-crystal width radial bins with minimal interpolation of irregularly spaced data. In the regions where DOI does not increase sampling density (chords normal to crystal faces), fine radial sinogram binning leads to zero efficiency bins if uniform angular binning is used. These zero efficiency sinogram bins lead to streak artifacts if not corrected. To minimize these unnormalizable sinogram bins we use two angular binning schemes: Fixed Width and Natural Width. Fixed Width uses a fixed angular width *except* in the problem regions where appropriately chosen widths are applied. Natural Width uses angle widths which are derived from intrinsic detector sampling. Using a modified filtered-backprojection algorithm to accommodate these angular binning schemes, we reconstruct artifact free images with nearly isotropic and position independent spatial resolution. Results from Monte Carlo data indicate that we have nearly eliminated image degradation due to crystal penetration.

I. INTRODUCTION

We are developing high resolution PET cameras optimized for breast and axillary node imaging [1]. The proposed camera is rectangular in shape and the imaging field extends to the front faces of the detectors. It is designed to operate without septa. The geometry of the camera exacerbates two problems in PET: radial elongation due to crystal penetration and image reconstruction from irregularly sampled sinograms.

Radial elongation, the degradation of image resolution caused by the penetration of the 511 keV photons into detector crystals, has limited the useful field of view (FOV) of PET cameras to regions close to its center. The effect of crystal penetration is small in these regions since the photons enter the crystals at angles close to normal. Point source resolution is degraded by up to a factor of three at distances of half the radius of circular tomographs (where an incident 511 keV photon can penetrate the crystals at 30°) [2]. Measurement of the depth of interaction of the 511 photons within the crystal has long been known to be a solution to this problem. Several

detector designs have attempted to incorporate methods measuring DOI [3-9]. With accurate measurement of DOI, radial elongation ceases to be a problem and the useful FOV encompasses the entire region bounded by the detector modules. However, little work has been done on how to best incorporate the DOI information into the reconstruction algorithm.

The extension of the FOV to include the entire region of the camera accentuates of the problem of reconstructing images from irregularly sampled sinograms. Filtered-Backprojection (FBP), a common reconstruction algorithm for PET because of its speed and simplicity, assumes that sinogram data are sampled regularly in the radial direction and at uniform angular increments. Sinograms from circular-PET cameras are in good agreement with these assumptions provided that the FOV from which sinogram data are taken is limited to the central region of the cameras. Our proposed detector geometry violates both these assumptions. Radial sampling is only approximately regular when chords are defined between opposite sides (banks) of the camera. In addition, angular sampling is not regular.

Previous works have addressed the issue of irregular sampling in PET cameras. Camera motion which is employed to increase the sampling density [10,11] and non-circular camera geometries [12] result in irregular sampling of the sinogram. The sampling issue is often addressed by rebinning the acquired data into regularly sampled sinogram bins and interpolation is often required to achieve evenly spaced sampling. This, however, effectively increases the radial bin width of the sinogram, often degrading spatial resolution. The DOI information of our proposed camera increases the sampling density without camera motion allowing us to rebin our data with minimal interpolation. However, as we shall show, while data in our camera can be binned in regular radial bins, we cannot bin them in completely regular angular bins.

In this paper, we explore FBP-based reconstruction algorithms for this detector geometry. We limit our discussion to 2D schemes with the intention of extending successful methods to 3D. In particular, we investigate two schemes: one whose angular sampling is based on the grossly nonuniform pattern obtained from a rectangular camera with discrete detectors and one that is as close to uniform sampling as possible. DOI information is essential to these schemes as the challenge is to exploit it where it increases sampling density while appropriately treating the sinogram regions where it does not. We shall show that measurement of the DOI allows stationary tomographs with discrete crystals to obtain high resolution imaging within a FOV that encompasses the entire region enclosed by the detectors.
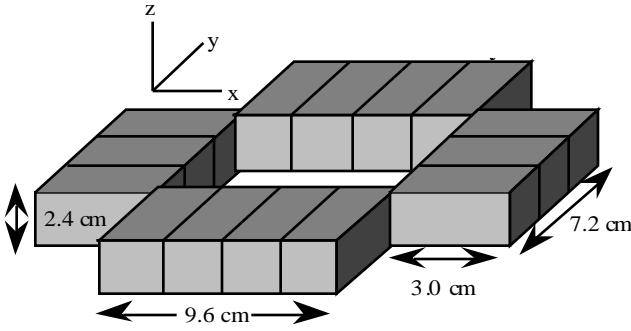
Figure 1. Simplified geometry showing modules. Each module consists of an (8x8) array of (3x3x30) mm³ crystals.

II. SIMPLIFIED CAMERA

A. DETECTOR CONFIGURATION AND SIMULATION

In order to understand the sampling of our proposed camera geometry, we first simulate a simplified camera composed of detector elements with 1.2 cm attenuation length and 100% photoelectric interaction cross-section. The geometry of the simplified camera is shown in figure 1. It is composed of 14 modules, each an (8x8) array of (3x3x30) mm³ crystals, a common photomultiplier tube (PMT) for timing and energy discrimination and a photodiode array (PD) for crystal of interaction identification. Only the 8x8 crystal blocks are shown in figure 1. We assume that light-sharing between the two photodetectors allows us to measure DOI [5]. The patient port is 9.6 cm by 6.0 cm. In the corners, there is 0.6 cm overlap between detector banks to avoid gaps between detector modules. The camera is designed to allow the long banks to move in order to accommodate subjects of varying breast sizes but we shall present work only for the dimensions above. The simulation assumes collinear photons and no positron range. Scatter in the object in the FOV is not included. The simulation is fully 3-dimensional but the reconstructions discussed in this paper are limited to 2D and thus cross plane events are not considered. For these simulations, the measured interaction depth is assumed to be the true DOI, smeared by a Gaussian distribution of fixed width of 0.0 mm, 5.0 mm or 10.0 mm FWHM.

B. SAMPLING DENSITY

Chords without DOI are defined by connecting the front faces of crystals (figure 2). The intrinsic sampling density in sinogram space of the simplified camera without DOI is shown in figure 3(A). The geometry intrinsically leads to irregular sampling of the tomographic data, both in the radial sinogram
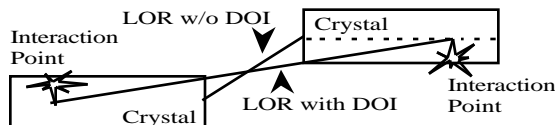

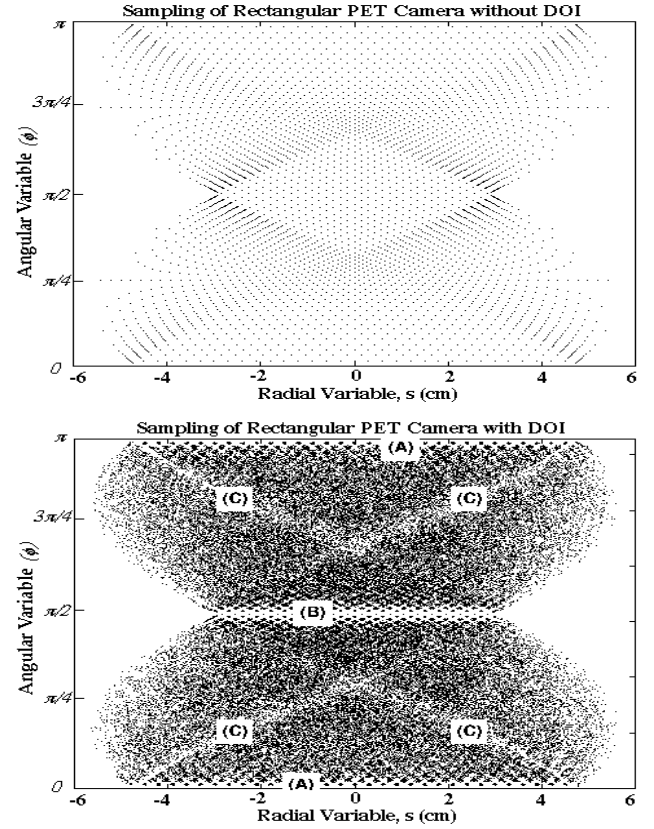Figure 2. Definition of Lines of Response (LOR) for events with and without DOI information.

Figure 3. (A) Sampling of the simplified camera from chords formed by connecting front faces of crystals. (B) Scatter plot of 200K coincidences detected by the simplified camera from a flood source. The true DOI is used to calculate the chord parameters.

coordinate, s, and the angular sinogram coordinate, ϕ. The field of view fills a region of sinogram space that resembles an hourglass. The irregularity of the sampling is readily apparent, even at the $s = 0$ line where the sampling would be regular if the camera were circular.

In contrast, chords with DOI are defined as connecting the photon interaction points perpendicularly projected onto the long axis of the crystals. This is also shown in figure 2. Figure 3(B) shows the sampling of the simplified detector if the true DOI is measured (0 mm FWHM). This scatter plot is produced by the Radon coordinates of events from a simulated flood source. There are several distinct regions in the sinogram. Regions (A) and (B), near $\phi = 0$ and $\phi = \pi/2$ respectively, represent chords formed by photons normally incident on the crystal faces. The DOI provides no new information because interactions that occur in the same pair of crystals but at different depths are mapped to the same chord and thus are degenerate. Sampling in these regions is almost identical to figure 3(A). Note that DOI improves the sampling significantly even at small angles from $\phi = 0$ and $\pi/2$. Regions (C), the slightly less dense areas that cross the hourglass, represent chords formed by crystals from corners of the rectangle where there is less detection material. This efficiency loss can be corrected by normalization. The rest of the sinogram exhibits high sampling density.
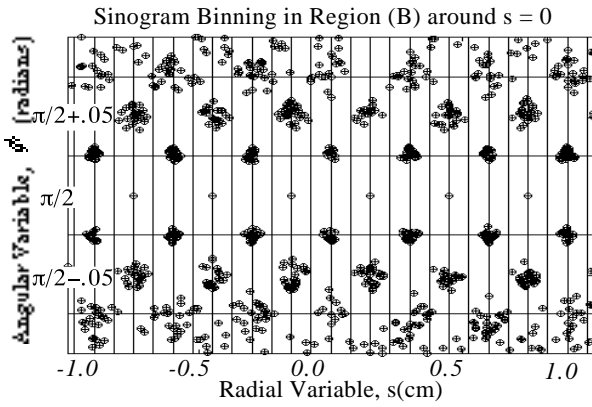
Sinogram Binning in Region (B) around s = 0

Figure 4. Sinogram binning in Region (B), $\phi \sim \pi/2$.

Natural Width and Fixed Width Angular Binning Schemes

Figure 5. NW and FW bin widths as a function of sampling angle.

C. SINOGRAM PARAMETERS

The speed and simplicity of FBP make it a convenient choice as a reconstruction algorithm for our proposed camera. In order to reconstruct our sinograms using FBP, we need to address the camera's irregular sampling. As shown in figure 3(B), continuous DOI all but removes the concern about irregular sampling. Discrete sampling only occurs in regions (A) and (B), which from hereafter we will call "the problem regions". The high sampling density of the simplified camera allows the use of quarter-crystal width (0.75 mm) radial bins throughout most of the sinogram. The choice of small bins allows us to maximally use the DOI information while the choice of regular sampling in the radial variable, s, allows us to use the Fast-Fourier Transform (FFT) in filtering the sinograms. This choice of sinogram bin size leads to empty (zero efficiency) sinogram bins *only* near the problem regions *and only when we sample at regular angular increments.*

For the same reason that we use small radial bins, namely to take full advantage of the DOI information, we would like to use small angular bins to sample the variable ϕ. However we need to use carefully selected angular widths around the problem regions in order to avoid zero efficiency sinogram bins which lead to severe streak artifacts. We choose small angular bin widths in all the regions of the sinogram *except* around the problem regions where we use the angular widths dictated by the geometry. We have modified the FBP algorithm to accommodate this choice of variable angular bin widths by multiplying each projection by a factor that is proportional to the angular width $\delta\phi$. Equation (1) describes this procedure where f is the approximated image intensity at the current pixel (x_i, y_j), F_n the nth of N filtered projections, r_{ij} the distance from the center of the tomograph to the current pixel, and $\delta\phi_n$ the angular width of the nth projection. This factor is ignored in current FBP reconstructions because it is a constant when the projections are taken at equal angular intervals.

$$\tilde{f}(x_i, y_j) = \sum_{n=0}^{N-1} \hat{F}_n \left(r_{ij} \cos\tfrac{n\pi}{N} + r_{ij} \sin\tfrac{n\pi}{N} \right) \, \delta\phi_n \quad (1)$$

Without penetration, the predefined angular bin widths in the problem regions are defined by the crystal widths and dimensions of the camer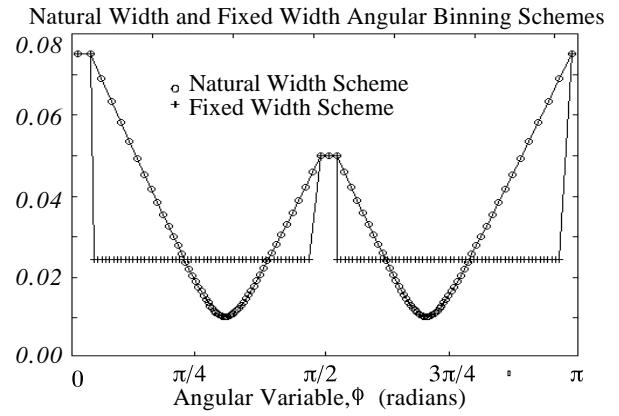a. With penetration and DOI, these widths are slightly modified. Figure 4 is an expansion of region (B) in figure 3(B) with s [-1.0,1.0]. The boundaries are chosen to bisect the clusters of points, yielding $\delta\phi_{\pi/2} = 0.050$. A similar procedure used around $\phi = 0$ requires that $\delta\phi_0 = 0.075$. These values are rounded to the nearest thousandth for simplicity. Figure 4 also shows the quarter-crystal width radial binning and the chosen angular binning in region (B) near $s = 0$ and $\phi = /2$. All of the sinogram bins are populated with the exception of the degenerate chords which lie on bin boundaries. A similar pattern (but with different spacing) occurs at $\phi = 0$. Half of the events from these chords are assigned to each of the bins upon whose boundaries they lie. This simple procedure of minimal interpolation leaves no unpopulated sinogram bins.

We construct two angular schemes to bin the events in the regions of dense sampling. The Natural Width scheme (NW) uses half the widths of the intrinsic sampling angles of the camera at $s = 0$ (figure 3(A)). The widths are then smoothed (except at 0 and /2). The Fixed Width scheme (FW) uses a fixed angular width in the densely sampled regions. At the problem regions, we use three angle bins with the predetermined widths. This gives us a total of 120 angular bins for both binning schemes. Figure 5 shows the angle bin widths as a function of sampling angle for both NW and FW binning schemes.

D. RECONSTRUCTED IMAGES AND RESULTS

Before reconstruction, the sinograms are normalized to correct for sampling and geometric efficiency variation of the camera. The normalization is calculated by comparing a flood source sinogram with the Radon Transform of a box of the appropriate dimensions. We use filtered backprojection with a ramp filter for reconstruction. In the FW angular binning scheme, the projection data with the wider widths at $\phi = 0$ are backprojected three times with 1/3 of the value at -0.075/3, 0 and 0.075/3. The same is done for the other two wider width projection data on either side of $\phi = 0$. Similarly, the projection data with the wider widths at $\phi = /2$ are backprojected twice with 1/2 of the value at /2-0.050/2 and /2+0.050/2. The same is done for the other two wider width projections data on either side of $\phi = /2$. The widths at $\phi = 0$ and $\phi = /2$ are approximately thrice and twice the small fixed width respectively.
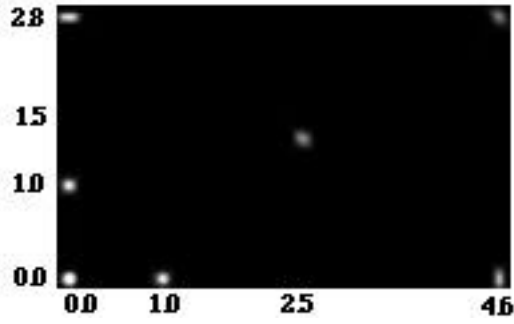
Figure 6. PSF at various locations of the camera. The top right quadrant is shown with the left bottom source at the center of the FOV (0,0) .

PSF Resolution for Various DOI Resolution			
Location	0 mm	5 mm	10 mm
(0.0, 0.0)	1.74(0.06)	1.90(0.05)	1.90(0.08)
(1.0, 0.0)	1.73(0.04)	2.15(0.13)	2.51(0.28)
(0.0, 1.0)	1.74(0.05)	2.17(0.04)	2.52(0.22)
(2.5, 1.5)	2.03(0.15)	2.35(0.06)	2.67(0.10)
(4.6, 0.0)	1.85(0.45)	2.81(0.12)	2.70(0.33)
(0.0, 2.8)	1.83(0.46)	2.70(0.08)	2.50(0.09)
(4.6, 2.8)	2.05(0.35)	2.51(0.14)	2.50(0.15)

Table 1. PSF Resolutions(mm) at various locations in the simplified detector for various uncertainties of the DOI (FWHM). The values in the parentheses are the variation in the value of the FWHM around the PSF.

Figure 6 shows a set of reconstructed images of point sources of equal intensities in various positions in the FOV. Perfect DOI resolution was assumed in the data and the FW angular binning scheme was used during reconstruction. Shown is the top right quadrant of the camera with the center of the FOV at (0,0). Table 1 lists the resolutions of the PSF. The variation in the number gives an indication of the symmetry of the PSF, *i.e.* the smaller the variation, the more circular the shape. The shapes of the PSF vary from circular at the center of the FOV to elliptical at the corners and near the edge. The PSF's near the edge have FWHM dimensions of 2.5 mm along the long axis and as small as 1.0 mm along the short axis. The long dimensions are consistent with a 3 mm crystal width while the short dimensions are the result of the DOI information. The apparent variation in the intensity of the sources is consistent with the variation in their FWHM's. ROI's drawn around each point source have equal activity.

We have shown that non-uniform angular sampling can be employed in a FBP-based reconstruction algorithm. We do not observe significant differences between the images reconstructed with the FW versus NW angular binning schemes as long as sampling in the problem areas is done using the predetermined widths. Hereafter we will present images reconstructed with the FW binning scheme, although
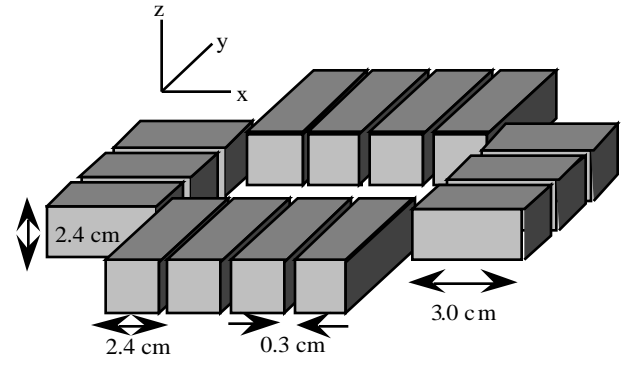

Figure 7. Realistic Detector Geometry.

we have verified that indistinguishable results are obtained with the NW binning scheme.

III. REALISTIC CAMERA

A. DETECTOR CONFIGURATION AND SIMULATION

Having developed a reconstruction algorithm for a simplified detector, we now add real world effects into the simulation. We include 0.5° FWHM Gaussian acollinearity between the photons and model fully-3D Compton scattering in the detector modules. We use the properties of LSO [13] to model scattering and attenuation. When energy is deposited in more than one crystal, as in the case when the 511 keV photon Compton scatters outside of the initial crystal, the crystal with the largest signal is chosen to be the crystal of interaction. Patient scatter in the FOV and positron range are not simulated. Reconstructions are limited to 2D so cross plane events are not used. The overall energy resolution is 17% FWHM at 511 keV.

We determine the DOI by measuring the light-sharing between the PD and the PMT signals when a photon deposits energy in a crystal [5]. The depth is determined by calculating a depth estimator Γ, defined as the ratio of the PD signal and the sum of the PD and the PMT, which varies linearly with the DOI. Γ is assumed to vary from 0.75 to 0.25 across the 3.0 cm crystal length. From Γ, the depth is calculated and discretized into one of eight DOI bins to model DOI measurement resolution. Reference [14] reports on the characterization of modules measuring DOI with this method.

In addition to the effects above, we also place one crystal width gaps between our detector modules. We anticipate these gaps in our proposed camera due to packaging limitations. The 2D acceptance of the camera drops by 10% due to the gaps between modules. Figure 7 shows the geometry of the realistic camera.

B. SAMPLING DENSITY

Figure 8 shows the sampling density of the realistic detector. The discrete DOI bins lead to an increase in the degeneracies in the sinogram (different chords that lie on the same point in sinogram space). The 3 mm gaps between the modules lead to unsampled x-shaped regions around $\phi = 0$ and
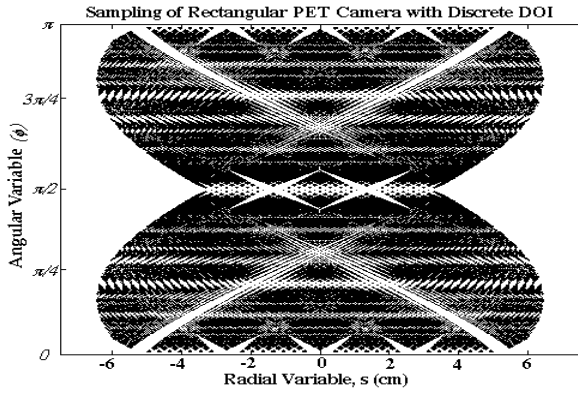
Figure 8. Sampling of the realistic camera. The sampling points are calculated from chords formed by connecting each DOI bin in each crystal with DOI bins from other crystals.

/2. The gaps in the corners result in unsampled regions around the (C) region of figure 3(A). DOI information minimizes the effect of the module gaps as the unsampled regions would have covered more of the sinogram if DOI were not measured.

C. SINOGRAM PARAMETERS

We wish to reconstruct using a method similar to that developed for the simple detector in spite of fact that the real-world effects exacerbate the sampling problems previously observed. The distribution of unsampled regions in the sinogram is such that there is not a set of angular bins (such as the FW or the NW) that will easily eliminate zero efficiency bins. In addition, the locations of the poorly sampled regions depend on the distance between the opposing detector banks which is adjusted for each patient. It would be desirable to use an algorithm which is not sensitive to the changing camera dimensions.

Many of these problems are caused by DOI discretation. We address this by adding noise to the calculated and discretized DOI to make it continuous again. Since the interaction point is assigned to the center of a DOI bin, we add a length to the DOI drawn from the flat distribution [-1.875,+1.875] cm (30 cm/8 DOI bins). The DOI takes a *continuous random value within the boundary discretized DOI bins*. The effect is to smooth the sinogram: more where it needs it and less where it does not. The procedure results in a sinogram with which we can again use the same angular binning schemes that we determined for the simplified camera. The dimensions of the realistic camera are slightly larger than the ideal one but the difference result in only a small change in the predetermined angles and widths are these angles.

The reconstruction of the sinogram of the realistic camera is essentially the same as in the simplified camera except that in the realistic camera, zero sinogram bins persist even after the redistribution of sinogram data between radial bins that was described in section II.D. These zero efficiency sinogram bins are the result of gaps in the corners of the camera, between adjacent detector banks. The zero sinogram bins resulting from the gaps between modules of the same bank are eliminated by
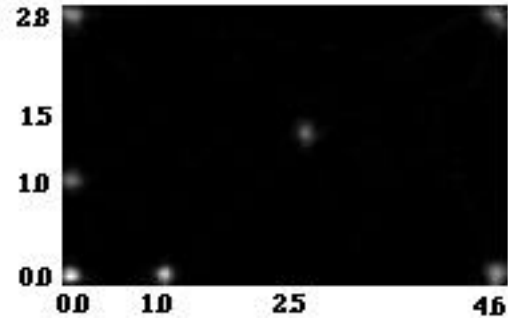

Figure 9. Reconstructed Point sources within the realistic camera. Shown is the top right quadrant of the FOV.

Location	PSF FWHM
(0.0, 0.0)	1.92(0.16) mm
(1.0, 0.0)	2.14(0.13) mm
(0.0, 1.0)	2.37(0.13) mm
(1.5, 2.5)	2.42(0.10) mm
(4.6, 0.0)	2.81(0.21) mm
(0.0, 2.8)	2.44(0.22) mm
(4.6, 2.8)	2.79(0.23) mm

Table 2. PSF Resolution (mm) at various locations in the realistic camera. The values in the parentheses are variations of the FWHM.

the addition of noise to the DOI. To remedy this situation, we use the Iterative Reconstruction Reprojection (IRR) [15,16] to estimate missing data. The IRR algorithm first reconstructs the image from the incomplete sinogram and then, using *a priori* information in the form of constraints, forward projects the reconstructed image into the gaps to estimate the values of the missing information. We use the positivity constraint (*i.e.* set all negative pixels to zero) in the intermediate images as our *a priori* information. Iteration of this procedure gives the final image.

D. RECONSTRUCTED IMAGES AND RESULTS

Figure 9 shows the reconstructed image of point sources in the same location as in the ideal camera, again reconstructed using the FW angular binning scheme. We performed only one iteration of the IRR algorithm since the image quality did not change dramatically with subsequent iterations. Table 2 lists the FWHM of the point sources at various location in the FOV of the realistic camera. The apparent differences in intensity of the point sources are due to the variation in the sizes of the reconstructed PSF. The intensities are proportional to the inverse of the square of their standard deviation. ROI's placed around these points yield identical activities.

Figure 10 shows a reconstruction of three extended sources and a point source. The image represents the entire FOV of the camera. We simulated a circle and two ellipses of various activity at various locations in the FOV. The circle has a radius of 0.50 cm while the semininor and semimajor axes
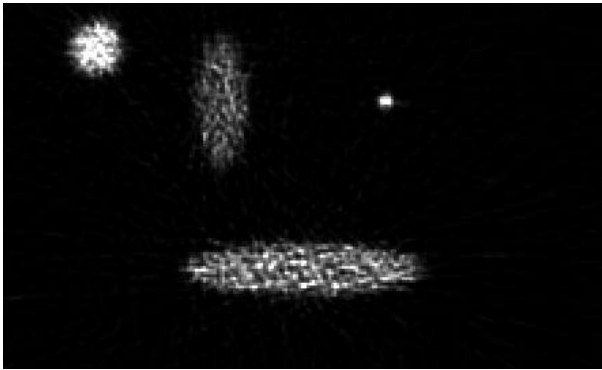
Figure 10. Reconstructed extended sources within the realistic camera (a circle, two ellipses and a point source). Image represents the entire FOV of the camera.

respectively of the ellipses are (0.50,1.25) cm for the vertical ellipse and (0.50,2.25) cm for the horizontal ellipse. The simulated relative activities, in the order circle:vertical ellipse:horizontal ellipse are 1.00:0.60:0.73. The image represents 10^6 events. We use a sharp filter filter for the reconstruction. The shapes of the source structures are sharp and their activities are relatively constant within their boundaries. The relative activities are consistent with the inputs to the simulation. We have included a point source to the right of the vertical ellpise. It has a reconstructed FWHM of 2.30(0.20) mm consistent with Table 2.

IV. CONCLUSION

We have developed reconstructions algorithms for data from PET cameras with irregular sampling and depth of interaction measurement capability. We use small and even radial binning to exploit the high sampling rate of the camera which necessitates variable-width angular binning schemes (FW and NW). We use a modified filtered backprojection technique to accommodate the irregularity in the angular sampling. The results indicate that the FW scheme gives qualitatively similar results as the NW scheme. Since discretized DOI can lead to unsampled bins, we add a small random number to the measured DOI to make it approximate a continuous variable. In the case where gaps in the camera lead to missing sinogram information, we use the IRR algorithm to approximate the missing information. The reconstructed images of point sources and extended phantoms are artifact free. The point sources are essentially isotropic and have FWHM's that vary from 1.9 mm to 2.8 mm depending on its position in the FOV. We do not observe the adverse effects of radial elongation in the images.

V. ACKNOWLEDGMENTS

VI. REFERENCES

[1] Moses WW, Budinger TF, Huesman RH, et al. "PET camera designs for imaging breast cancer and axillary node involvement." J. *Nucl. Med. 36*: pp. 69P, 1995.

[2] W.W. Moses, P.R.G.Virador, S.E. Derenzo, R.H. Huesman and T.F. Budinger, "Design of a High-Resolution, High-Sensitivity PET Camera for Human Brains and Small Animals," *IEEE Trans. Nucl. Sci.,* vol NS-44, pp. 1487-1491, 1997.

[3] J.S. Karp and M. Daube-Witherspoon, "Depth of interaction determination in NaI(Tl) and BGO scintillation crystals using a temperature gradient", *Nucl. Instrum. Methods,* vol. A-260, pp. 509-517, 1987.

[4] J.G. Rogers, C. Moisan, E.M. Hoskinson, et al., "A practical block detector for a depth-encoding PET camera," *IEEE Trans. Nucl. Sci,* vol. NS-43, pp. 732-738, 1991

[5] W.W. Moses, S.E. Derenzo, C.L. Melcher, at al., "A room temperature LSO/PIN photodiode PET detector module that measures depth of interaction," *IEEE Trans. Nucl. Sci.,* vol. NS-42 pp. 1085-1089, 1995.

[6] P. Bartzakos and C.J. Thompson, "A depth-encoded PET detector," *IEEE Trans. Nucl. Sci.,* vol. NS-38, pp. 732-738, 1991.

[7] W. Worstell, O. Johnson and V. Zawarin, "Development of a high-resolution PET detector using LSO and wavelength shifting fibers," Proceedings of the 1995 IEEE Nuclear Science Symposium and Medical Imaging Conferenc pp. 1757-1760, San Francisco.

[8] R. Miyaoka, T.K. Lewellen, et al., "Design of a depth of interaction (DOI) PET detector module," *submitted to IEEE Trans. Nucl. Sci.,* vol. NS-44 1998.

[9] Y. Shao, S.R. Cherry et al., "A study of depth of interaction with Multi-Anode PMT and single channel photodiode", *submitted to IEEE Trans. Nucl. Sci.,* vol NS-44, 1998.

[10] Dagher, A., Thompson, C.J., "Real-time data rebinning in PET to obtain uniformly sampled projections", *IEEE Trans. Nucl. Sci.,* vol NS-32, pp. 811-817, 1985.

[11] R. H. Huesman, S.E. Derenzo, and Budinger, T.F., "A two position sampling scheme for positron emission tomography", Nuclear Medicine and Biology, Proceedings of the Third World Congress of Nucl. Sci. and Biol, vol. 1 pp. 542-545, 1982

[12] Muehllehner, G., Karp, J.S., Guvenis, A., "A method for reconsturcting images from data obtained with a Hexagonal Bar Positron Camera", *IEEE Trans. Med. Imag.,* vol MI-4, pp. 134-138, 1985

[13] C. L. Melcher and J. S. Schweitzer, "Cerium-doped lutetium orthosilicate: A fast, efficient new scintillator," *IEEE Trans. Nucl. Sci.,* vol NS-39, pp. 502-504, 1992

[14] J.S. Huber, W.W. Moses, S.E. Derenzo, M. Ho, M.S. Andreaco, M.J. Paulus and R. Nutt, "Characterization of a 64 Channel PET Detector Using Photodiodes for Crystal Identification", *IEEE Trans. Nucl. Sci.,* vol NS-44, pp 1197-1201, 1997

[15] B.P. Medoff, W.R. Brody, M. Nassi and A. Macovski, "Iterative Convolution Backprojection Algorithms for Image Reconstruction form Limited Data," *J. Opt. Soc. Am.,* vol 73-11 pp. 1493-1500, 1983

[16] Ollinger J.M., Karp, J.S.. "An evaulation of three algorithms for reconstructing images from data with missing projections." *IEEE Trans. Nucl. Sci ,* vol NS-35, pp. 629-634, 1988